High-fidelity Aerostructural Optimization Studies of the Aerion AS2 Supersonic Business Jet

Nicolas Bons*, Joaquim R. R. A. Martins†, and Charles A. Mader‡
Supercritical Research LLC, Ann Arbor, MI, 48103

Matthew McMullen§ and Michelle Suen¶
Aerion Supersonic LLC, Palo Alto, CA 94303

The Aerion AS2 is poised to make supersonic transportation viable and drastically reduce transoceanic travel time. The design of a supersonic transport aircraft is challenging because experience with this type of aircraft is scarce. Achieving the required range at supersonic speeds requires a refined design with the best combination of aerodynamic and structural performance. Adequate transonic cruise performance is also required due to mission segments overland. To address these issues, we perform CFD-based aerostructural design of the Aerion AS2 supersonic business jet configuration. The aerostructural optimization simultaneously varies structural sizing and wing shape variables to maximize a combination of supersonic and transonic cruise ranges. We examine the design trades between these two ranges by generating sets of Pareto-optimal designs. Optimizations that include wing planform design variables achieve the best design trades, but maximizing supersonic range is particularly challenging. Overall, these initial results show that CFD-based multidisciplinary design optimization is fast enough that we can perform this type of extensive design exploration before the detailed design stage.

1. Introduction

Despite many technological advances, the speed of air transportation vehicles has remained at the high transonic range since the dawn of the jet age. One exception is the Concorde, which flew transatlantic routes at Mach 2 between 1976 and 2003. While it represented a tremendous achievement, the Concorde was never profitable and did not keep up with evolving emission standards and increasingly stringent noise regulations.

Since the Concorde, we have had decades of new technological developments in materials, propulsion, aerodynamics, and controls. In addition to these airframe technology developments, the design process has evolved dramatically. Modern computing makes it possible to represent the aircraft digitally and to perform computer simulations modeling virtually every aspect of the aircraft. With the advent of multidisciplinary design optimization (MDO), it is now possible to use numerical optimization to aid the design space exploration by making optimal tradeoffs between the relevant disciplines. Thus, one compelling question to consider is: What is the best design we can achieve for a supersonic transport today?

Even after accounting for the developments cited above, the economic viability of supersonic commercial transportation remains elusive. Developing a transonic transport aircraft is already an inherently risky endeavor from a financial point of view, let alone a supersonic one. However, because of the sustained long term growth of business aviation, with a preference for high-end, long-range aircraft [1], we believe the business aviation market is ready for a supersonic aircraft. Business jet customers overwhelmingly value speed, as evidenced by the higher cruise speeds compared to airliners (Mach 0.9 versus 0.85). An even higher increase to supersonic speed would effectively enable customers to buy time, a precious commodity that cannot usually be bought.

Aerion has been developing supersonic business jet designs since the early 2000s, unveiling their first design one year after the Concorde's retirement, and making innovations in modeling and design optimization [2–10]. A finalized design of the Aerion AS2 business jet that can transport 8–10 passengers at Mach 1.4 was recently unveiled [11]. A

---

*AIAA Student Member.
†Owner. Also Professor of Aerospace Engineering, University of Michigan. AIAA Fellow.
‡AIAA Senior Member.
§Aerospace Engineering Manager. AIAA Senior Member.
¶Aerospace Engineer. AIAA Member.

Fig. 1 Aerion AS2 supersonic business jet configuration

rendering of this configuration is shown in Fig. 1. It features a cranked-arrow wing planform and three engines, two of which are mounted under the wing. The AS2 aims to achieve a range of 4,200 nm at $M = 1.4$ and 5,400 nm at $M = 0.95$.

The success of the Aerion AS2 hinges on both environmental sustainability and performance. Environmental sustainability includes consideration for greenhouse gas emissions, sonic boom during cruise, and noise during the landing and take-off (LTO) cycle. While supersonic flight is inherently less efficient than subsonic flight and thus emits more carbon dioxide per passenger-mile, Aerion is planning to use pure biofuels to make the AS2 closer to carbon neutral. When it comes to the sonic boom, current regulations prevent supersonic flight over land. For that reason, we consider the performance at high-subsonic speed in this paper, in addition to the supersonic performance. However, it will be possible to cruise slightly above the speed of sound using *boomless cruise*, a technology developed and patented by Aerion [12]. This technology takes advantage of atmospheric refraction so that the boom produced by the aircraft cannot be heard on the ground. LTO cycle is another challenge for supersonic aircraft. To tackle this challenge, Aerion has partnered with General Electric Aviation, who is developing the Affinity engine. This engine is being designed to meet the upcoming Stage 5 environmental and noise standards.

The design of the AS2 wing is challenging because, in addition to performing optimally at the supersonic cruise condition, it must also have adequate performance at transonic and low-speed flight conditions. The design trades between these various conditions are not obvious, but can be informed by multipoint aerodynamic shape optimization [13, 14].

To tackle the performance challenge, we require state-of-the-art design methodologies. Because of the scarcity in previous knowledge on supersonic transport configuration design, such methodologies must be based on models that consider all the relevant physics. We address this need using the MACH framework, which was developed to perform multidisciplinary design optimization (MDO) with high-fidelity models for the aerodynamic and structural disciplines, that is, aerostructural optimization [15, 16]. Coincidentally, Martins et al. [17] demonstrated an early version of this methodology for the first time on an Aerion-inspired supersonic business jet configuration.

Aerostructural optimization in the MACH framework has several advantages relative to pure aerodynamic shape optimization. First, it accounts for the fact that the wing has different shapes at different flight conditions. Second, it makes it possible to remove the artificial thickness constraints that have to be enforced in aerodynamics-only optimization to prevent unrealistically thin designs. Third, by simultaneously optimizing the aerodynamic shape and structural sizing, aerostructural optimization can make the correct trade between aerodynamic and structural performance to maximize

the objective function that represents the ultimate performance metric. Finally, we can now make design trades by changing wing planform variables, since the optimal value for these strongly depend on design considerations from both aerodynamics and structures.

In this paper, we present aerodynamic shape and aerostructural design optimization studies of the Aerion AS2 configuration. We start by describing the MDO framework (MACH) in Sec. 2. In the aerodynamics-only studies (Sec. 3), we present the aerodynamic model and investigate the impact of enforcing a curvature constraint on the resulting shapes. In the aerostructural studies (Sec. 4), we present the structural model and show two sets of results: fixed planform (Sec. 4.1) and variable planform (Sec. 4.2). The trade studies are presented and discussed in Sec. 4.3, and we end with the conclusions in Sec. 5.

2. Methodology

In this work, we use the MACH framework for the high-fidelity aerostructural optimizations. This framework has been previously used for various studies, including conventional transonic transport aircraft [15, 18], the D8 double bubble configuration [19], morphing trailing edge wings [20, 21], and tow-steered carbon-fiber co mposite wings [22, 23]. Incidentally, an early prototype of the MACH framework (using different solvers, but featuring the coupled-adjoint approach described below), found its first application to the design of a supersonic business jet configuration inspired by an Aerion configuration [17].

MACH couples Reynolds-averaged Navier–Stokes (RANS) computational fluid dynamics (CFD) with a finite-element structural solver to compute the wing performance accounting for their actual in-flight shape due to static aeroelastic displacements [16]. In addition, it efficiently computes derivatives of aerodynamic force coefficients and structural stresses with respect to both aerodynamic shape and structural sizing variables. The derivatives are accurately and efficiently computed using a coupled-adjoint approach [16]. These derivatives can then be used to inform a gradient-based optimizer. The combination of the gradient-based optimizer and the coupled-adjoint method enables the simultaneous optimization with respect to hundreds of aerodynamic shape and structural sizing variables [15]. A diagram showing the modules and procedure of the MACH framework is shown in Fig. 2.
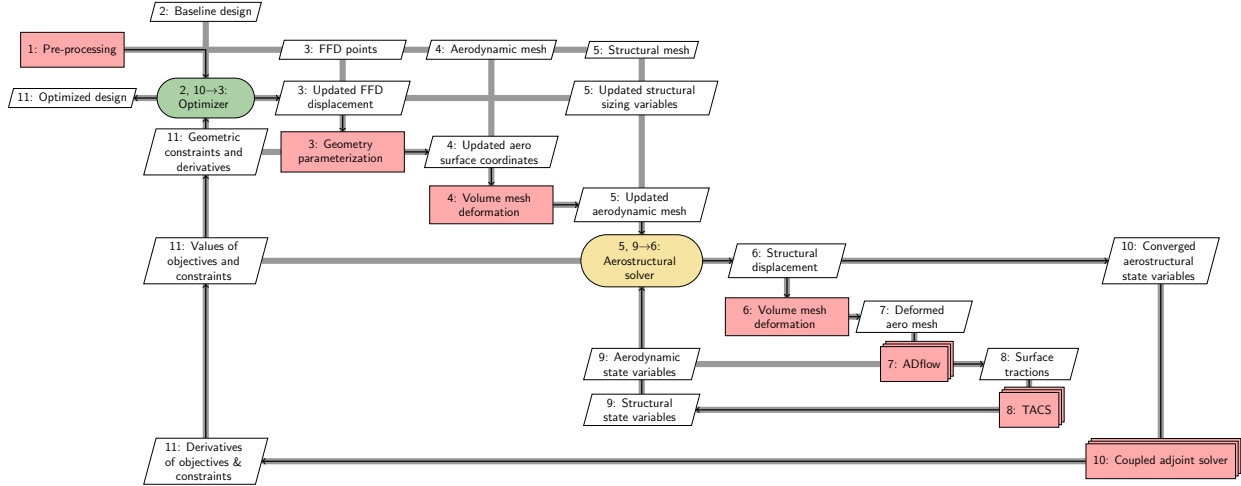

Fig. 2   MACH framework modules, data dependencies, and optimization procedure.

The aerodynamic solver used in MACH is ADflow [24], a second-order, finite-volume CFD solver. ADflow can solve Euler and RANS models on structured multiblock and overset meshes. In this work, we use the RANS model with the Spalart–Allmaras turbulence model. ADflow computes the aircraft aerodynamic loads and functions of interest—lift, drag, and moment—in the MACH aerostructural solver. ADflow efficiently computes derivatives of its functions of interest through a discrete adjoint approach, which was implemented through the selective application of automatic differentiation [25].

The structural solver in MACH is TACS (Toolkit for Analysis of Composite Structures) [26], which is an efficient parallel computational structural mechanics (CSM) solver that is particularly effective in the analysis of the thin-walled

structures that are typical in airframes. TACS computes the aircraft structural deformations and functions of interest—stress, buckling, and mass—in the aerostructural solver. Like ADflow, TACS uses an adjoint approach to efficiently compute derivatives of its functions of interest with respect to the design variables [26].

The coupling procedure for the aerodynamic and structural solver interpolates the structural displacements from the surface of the CSM mesh to the surface of the CFD mesh, and then extrapolates these displacements to the farfield of the CFD volume mesh. The framework uses a mesh warping algorithm that deforms mesh vertices based on an inverse distance weighting that preserves the quality of the mesh, thus preserving the accuracy of the CFD solution when applied to design iterations that significantly change the geometry [27].

The aerostructural solution procedure in MACH integrates the aerodynamic and structural solvers and mesh warping algorithm. The coupled solver uses a block Gauss–Seidel approach, wherein the aerodynamic loads from the CFD model are passed as tractions to the CSM solver, which computes the elastic deformation of the structure [16]. These deformations are interpolated to the wing surface by connecting each CFD surface node on the wing to the nearest CSM node through rigid links [28, 29]. As mentioned previously, the mesh movement algorithm then propagates the deformations on the wing surface to the farfield of the CFD mesh. This results in a new CFD mesh with a deflected wing profile, which is solved again to compute the updated aerodynamic loads. This procedure is then repeated until convergence. The aerostructural design derivatives are computed by solving the coupled adjoint for the aerodynamic and structural solvers. This allows us to compute design derivatives with respect to thousands of design variables for little additional cost relative to the aerostructural Gauss–Seidel solution [16]. The optimization problem is setup using pyOptSparse [30] *.

3. Aerodynamic Shape Optimization

Before proceeding with the aerostructural optimization, we performed a series of aerodynamic shape optimizations with fixed-wing planform. The aerodynamic model and design parametrization described here are reused for the aerostructural optimization in Sec. 4.

Our design optimization studies start from the initial configuration shown in Fig. 3. The wing planform has a cranked-arrow wing shape with an outboard leading edge sweep of 54 degrees. The fuselage features aggressive area ruling to reduce the wave drag at cruise conditions. The passenger cabin is located in the forward bulge.
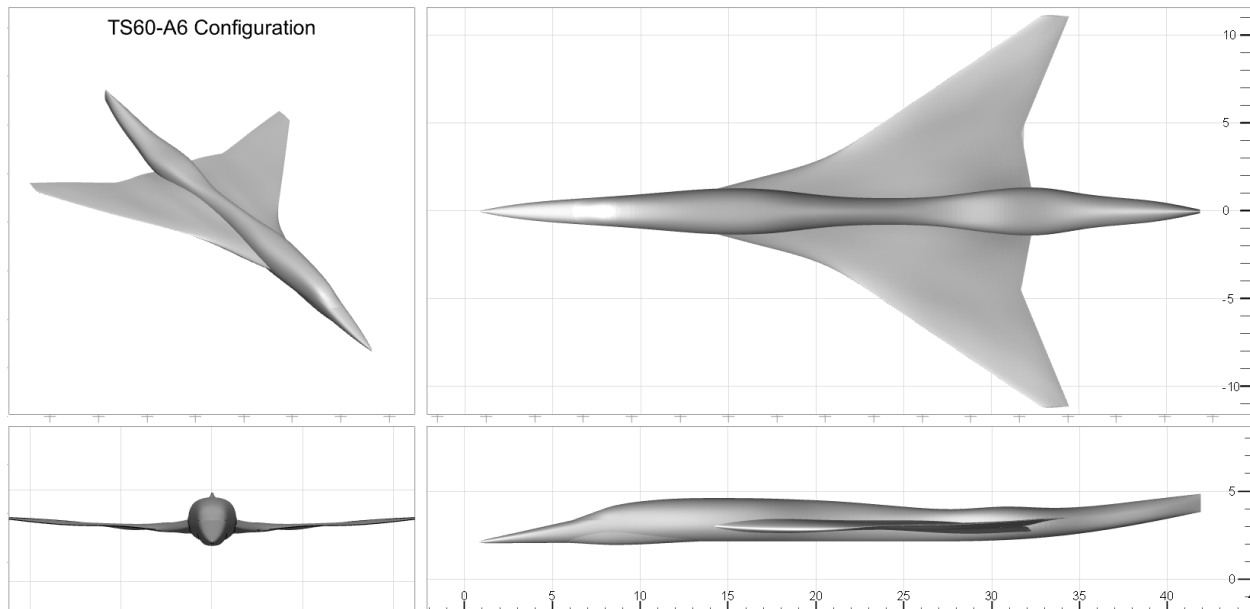

TS60-A6 Configuration

Fig. 3

The geometry shown in Fig. 3 excludes the vertical tail, horizontal tail, and nacelles, for simplicity. The vertical

---

*https://github.com/mdolab/pyoptsparse

and horizontal tails do not significantly affect the design trades of the present study except to add some drag. While the horizontal tail and its angle affect the trade between trim drag and other drag sources [31], these effects are small for the AS2 configuration. The lack of nacelles in this model also results in an underestimate of the total drag. Our preliminary studies that included nacelles have shown that it is essential to include the nacelles to get the optimal wing shape near the nacelles (taking advantage of favorable interference), but that this should not affect the wing planform shape significantly.

The CFD model consists of the structured overset mesh shown in Fig. 4. Two separate meshes are built for the fuselage and wing by extruding surface meshes with the hyperbolic mesh generator pyHyp. [†] We also generate a collar mesh around the wing-fuselage intersection with pyHyp. Then we assemble the three meshes to create the final mesh following the procedure detailed by Secco et al. [32]. The final mesh has 2.42 million cells.
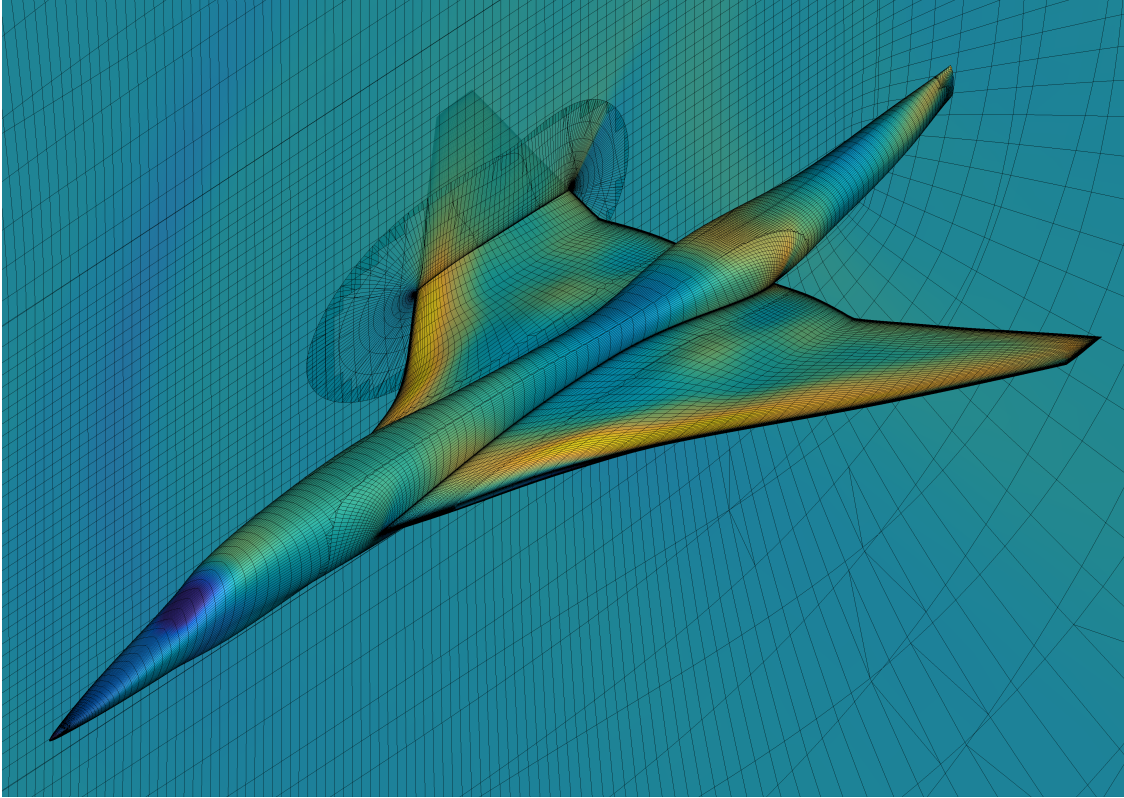

Fig. 4   The RANS equations are solved using an overset mesh with 2.42 million cells.

The objective of the aerodynamic shape optimization is to minimize the weighted sum of the drag coefficients for the supersonic and transonic flight conditions,

$$J = \beta C_{D_s} + (1 - \beta)C_{D_t}, \tag{1}$$

where β is the weighting factor.

The aerodynamic design variables consist of the angles of attack for each of the two flight conditions, the airfoil shape variables, and section twist variables, as listed in Table 1. The two angles of attack ensure that the lift coefficient for each cruise condition matches the corresponding target value.

The airfoil shape is controlled using the free-form deformation (FFD) volume shown in Fig. 5. The control points can move in the z direction, except for the ones in the four inboard chordwise rows, which are fixed. The total number of moving control points on the top and bottom surface is 198. The wing twist at six spanwise positions is controlled by rotating the corresponding set of FFD control points. The sections are prevented from shearing by constraining

---

[†]`https://github.com/mdolab/pyhyp`

	Function/variable	Description	Number
minimize	$\beta C_{D_s} + (1-\beta)C_{D_t}$	Objective function	1
w.r.t.	x_α	Angles of attack	2
	x_{twist}	Wing twist	6
	Δz	Wing shape (FFD)	198
subject to	$C_L = C_L^*$	Target lift coefficient	2
	$t/t_{\text{init}} \geq 1$	Thickness constraints	100
	$\Delta z_{\text{LE}_u} = -\Delta z_{\text{LE}_l}$	Fixed leading edge	11
	$\Delta z_{\text{TE}_u} = -\Delta z_{\text{TE}_l}$	Fixed trailing edge	11
	$K \leq 0.9 K_{\text{init}}$	Average curvature constraint	2

Table 1   Aerodynamic optimization problem objective, design variables, and constraints.

the control points at the leading and trailing edges. Finally, we constrain the thickness of the wing using "toothpick constraints" placed at various locations on the wing. These constraints are created by projecting a point to the upper and lower surface of the wing and then tracking the relative position of the points throughout the optimization. The user can choose to set the constraint as an absolute value or relative to the baseline value. A total of 30 thickness constraints are placed along the leading and trailing edges of the wing, preventing the thickness from decreasing at those locations. An additional 25 thickness constraints are distributed in the tip region of the wing, again preventing decrease in thickness from the original value. Three sets of 15 constraints are positioned along the front, mid, and rear spars. These constraints are set to not decrease below a value dictated from previous trade studies conducted by Aerion. In total, 100 thickness constraints are used in the aerodynamic optimization problem.
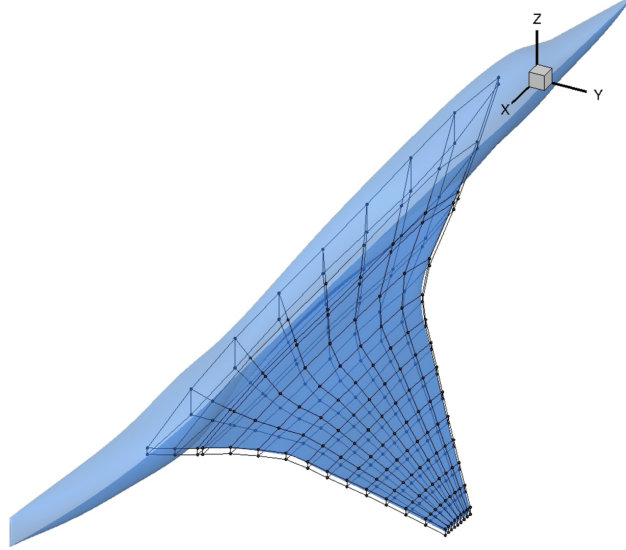

Fig. 5   Free-form deformation volume points used to parameterize the wing shape. The airfoil shapes are controlled by moving the points in the z direction.

Finally, we introduce a geometric curvature constraint in our optimizations, which was developed and applied in previous unpublished work [33]. The motivation for this curvature constraint is that some optimizations can yield

surfaces that are expensive or even impossible to manufacture due to high curvature. Thin wings with large chords, such as the ones considered here, are especially vulnerable to this issue.

At any point on a surface, there are two principal curvatures (the maximum and minimum curvatures of the surface at that point). These principal curvatures (k_1 and k_2) are computed using a discrete scheme based on central differences. We used the average of the two principal curvatures at each point,

$$\kappa = \frac{1}{2}\left(\kappa_1 + \kappa_2\right),\tag{2}$$

and then integrate this quantity over each surface to get

$$K = \iint_S \kappa^2 \, dS.\tag{3}$$

This integral is evaluated numerically on the upper and lower wing surfaces and these average curvatures are constrained such that

$$K \le r K_{\text{init}},\tag{4}$$

where K_{init} is the curvature of the initial shape and r is the ratio of allowed curvature relative to the initial value. The leading edge of the wing was excluded from the surface integral (3).

To examine the effect of curvature constraint, we performed aerodynamic optimizations for several values of r, with $\beta = 0.85$. The drag coefficient values at the transonic and supersonic conditions for the optimized configuration are plotted against r in Fig. 6. As expected, the optimized drag values decrease as the allowable average curvature increases. Both the transonic and supersonic drag values decrease sharply for $0.55 < r < 0.7$, but for $r > 0.9$, the drag values decrease by less than one count. Therefore, we decided to use $r = 0.9$ for all the other optimizations in this work.
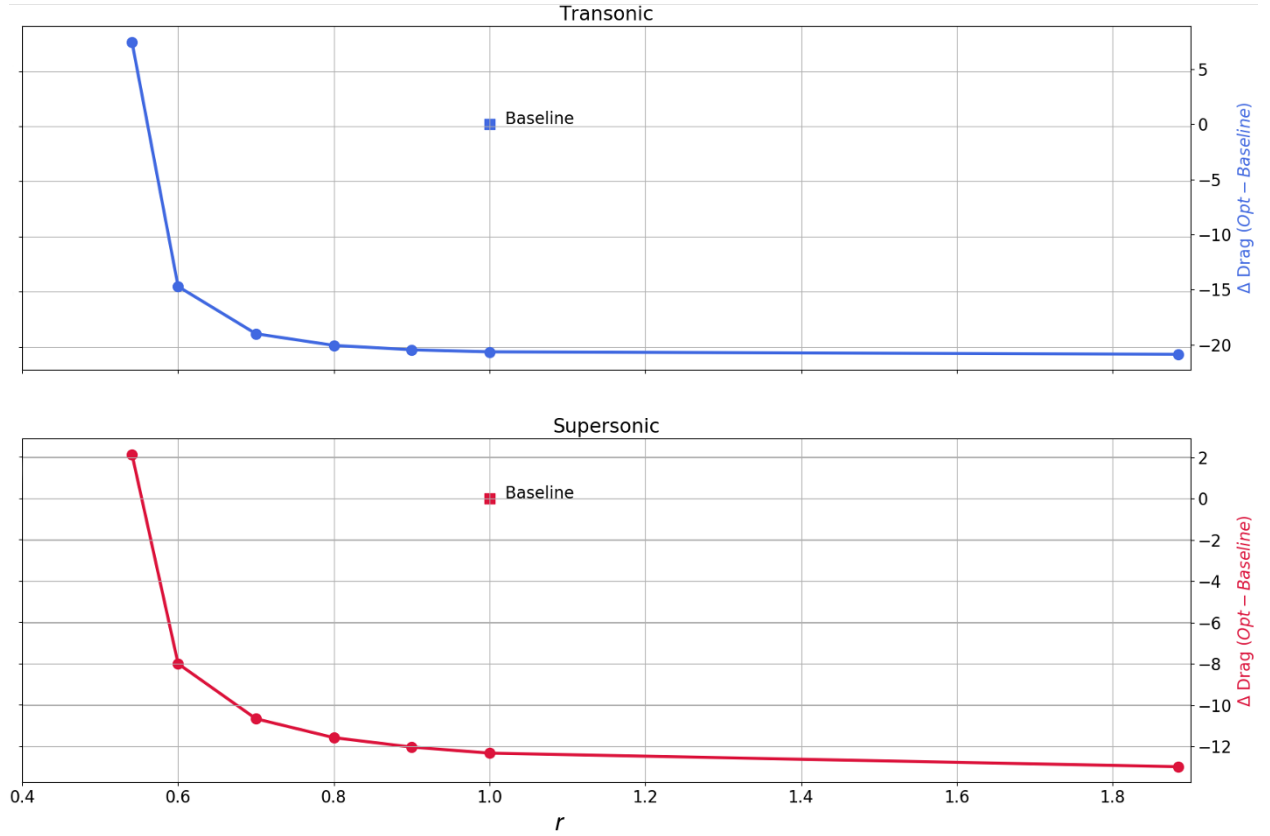

Fig. 6 The curvature constraint does not have a significant effect on either the transonic or supersonic drag of the optimized configurations for a relative curvature of $r > 0.9$.

The average curvature constraint was effective in limiting the local curvature of the optimized shape, as shown in Fig. 7. This figure does not show the front 10% chord of the surface because, as previously mentioned, the curvature was not constrained at the leading edge. The local curvature on the upper wing surface for the optimization with no curvature constraint (middle) generates various hot spots with high curvature. However, these hot spots do not appear in the optimization with the curvature constraint (right); although it has more curvature variation relative to the baseline, the local curvatures do not exceed the baseline values. The lower surface is not shown here, but it exhibits similar trends to the upper surface.
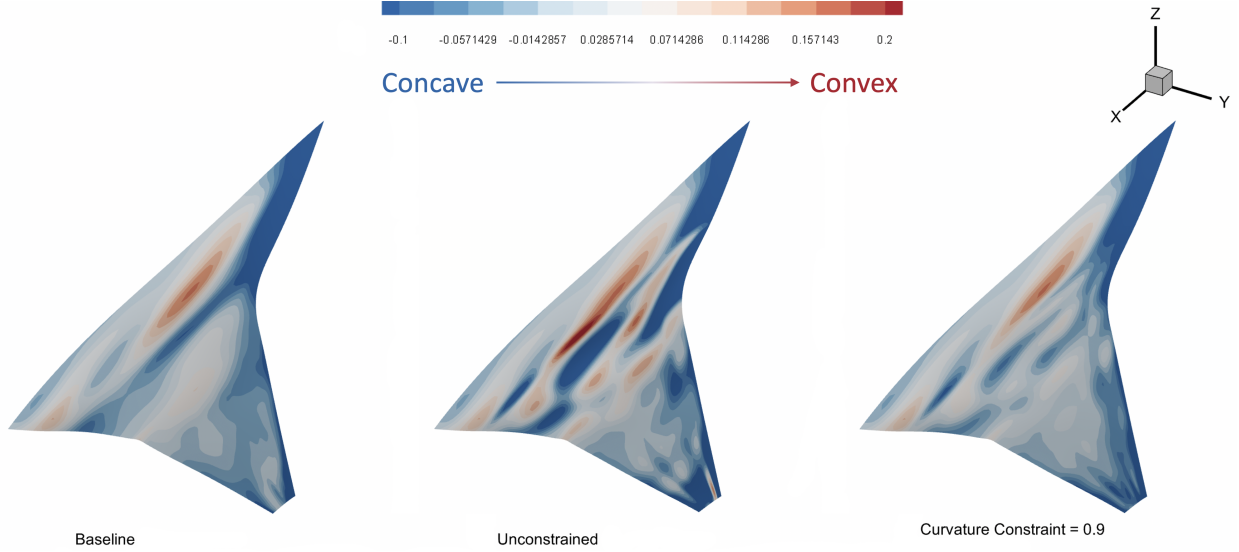

Fig. 7   Upper wing surface curvature of baseline design (left), curvature of optimized surface without curvature constraint (middle), and with relative curvature constraint of $r = 0.9$ (right).

To examine the curvature in more detail, we plot both spar shape profiles (Fig. 8) and airfoil profiles (Fig. 9). Again, we can see that the curvature constraint smoothed out the convexities and concavities that the unconstrained optimization generated. This smoothing is more pronounced in the chordwise curvature and contributes to smoother chordwise C_p distributions.

In the spar profiles, we can see a significant thickening in the mid and forward spars shown in Fig. 8. Since these optimizations do not include a volume constraint or structural considerations, this thickening must be for aerodynamic reasons. The most probable explanation is that this thickness is added to compensate for the lack of nacelles in our model. The baseline configuration was designed with an aggressive area ruling on the fuselage (see Fig. 3), but that was done accounting for the nacelles. This thickening is also evident in the airfoil profiles (Fig. 9).

We performed a series of aerodynamic-only shape optimizations (with the curvature constraint) for different values of β. We reserve the discussion of these results for the next section, where we compare them to the aerostructural optimizations.

4. Aerostructural Optimization

Similar to the aerodynamic shape optimization, the objective of the aerostructural design optimizations is to maximize a weighted combination of supersonic and transonic performance. In the aerostructural case, we need a performance metric that captures the correct tradeoff between drag and weight. Range is a useful metric, because it is crucial for the success of the Aerion AS2. Furthermore we want to study the trade between supersonic and transonic range, so the objective is

$$J = \beta R_s + (1 - \beta)R_t, \tag{5}$$

where each of the ranges are estimated using the Breguet range equation,

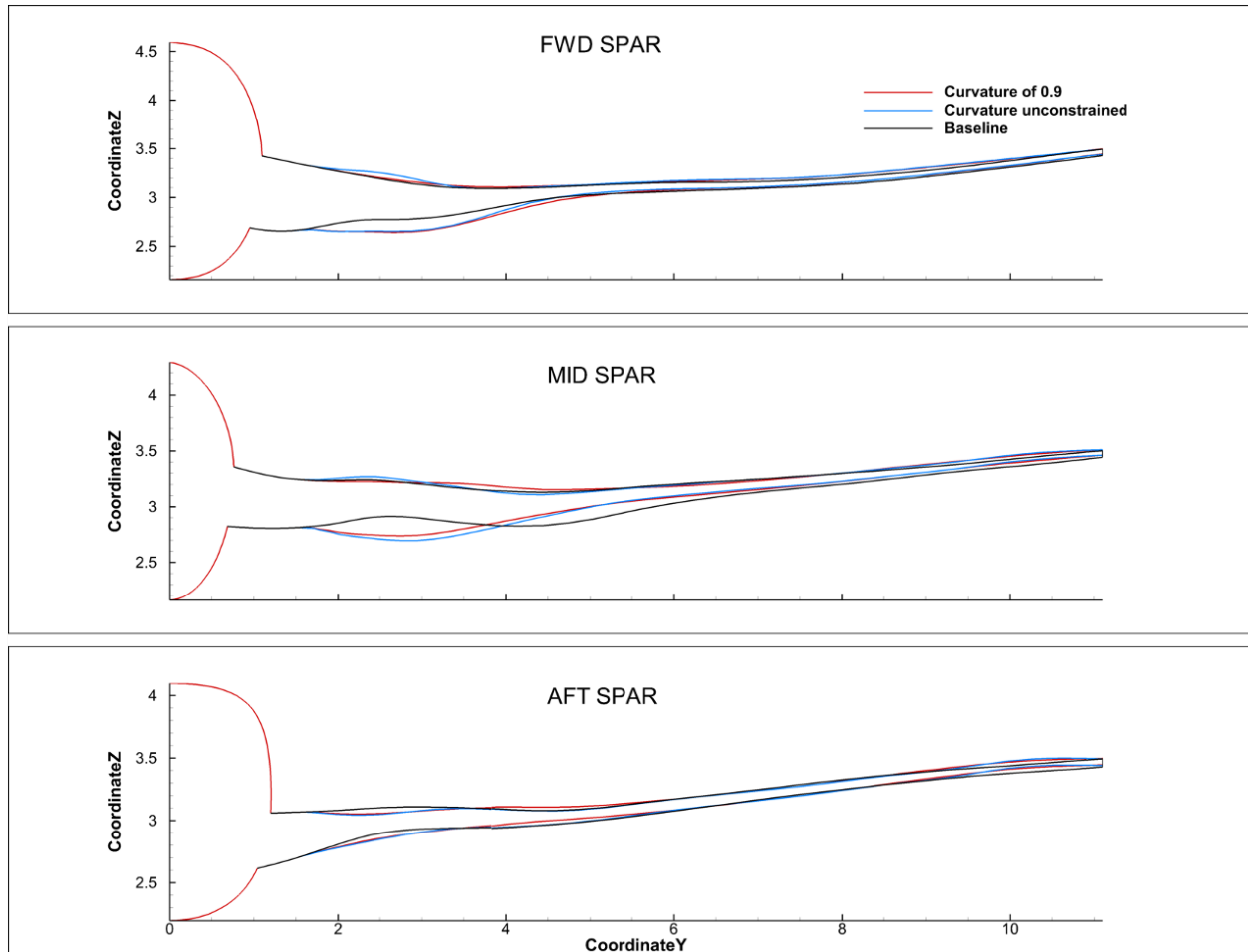$$R = \frac{V}{c} \frac{C_L}{C_D} \ln\left(\frac{W_i}{W_f}\right), \tag{6}$$

Fig. 8 **The inclusion of the curvature constraint smoothed out the spanwise profiles of the optimized configuration.**
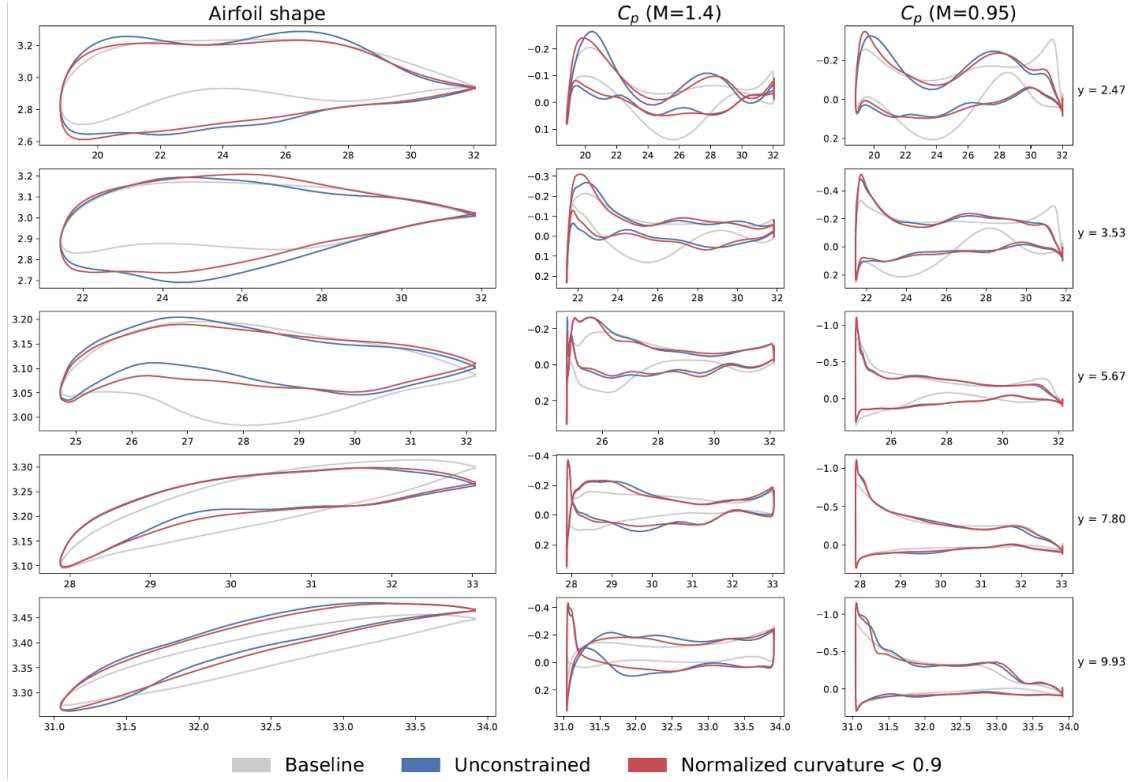
Fig. 9 The inclusion of the curvature constraint smoothed out the airfoil profiles of the optimized configuration.

where $\beta = 1$ would maximize solely supersonic range, and $\beta = 0$ would maximize only transonic range. Several optimizations with values of β between zero and one are performed to explore the trade between supersonic and transonic performance.

Each optimization iteration requires three aerostructural analyses: one supersonic and one transonic cruise condition for evaluating the two ranges, and a 2.5 g pull-up maneuver condition for which the structural constraints are enforced. Three angles of attack design variables ensure that the optimizer can satisfy the lift constraint at each flight condition.

The complete list of design variables and constraints is listed in Table 2. The design variables and constraints expand on the ones used for the aerodynamic shape optimization (Table 1). In an aerostructural optimization, we would usually enforce "lift equals weight" instead of target lift coefficients and include the altitude as a design variable. However, we decided to keep the target lift coefficients from the aerodynamic shape optimization to avoid having to account for variations in the engine specific fuel consumption.

As before, the geometric variables are implemented in the FFD volume shown in Fig. 5. For the last set of aerostructural optimizations, we add wing planform variables (span and taper) that move all the FFD points in the x-y plane to achieve the desired effect. To avoid adding other aircraft design considerations related to field and low-speed performance, we also force the wing planform area to remain constant through a constraint. In addition, the structural model is embedded in the FFD volume, so any changes applied to the volume directly deform the wingbox as well.

The structural wingbox features the spar-rib arrangement shown in Fig. 10 (left). The large bay is necessary to stow the landing gear. The material is carbon fiber reinforced polymer with a density of 1550 kg/m^3, Young's modulus of 62.1 GPa, Poisson's ratio of 0.045, and a yield strength of 280 MPa. The composite laminate properties are assumed to be isotropic in these studies.

The wingbox is discretized using 14,430 second-order MITC shell elements with 82,782 degrees of freedom, as shown in Fig. 10 (middle). The structural model uses a smeared stiffness approach to represent stiffened panels. Each panel is parametrized with four variables: panel thickness, stiffener thickness, stiffener pitch, and stiffener height, as shown in Fig. 10 (right). The values for these variables are then used to compute the *ABD* matrices for each panel. There are 224 panels parameterizing the skins, spars, and ribs, for a total of 566 structural sizing design variables. All

	Function/variable	Description	Number
maximize	$\beta R_s + (1 - \beta)R_t$	Objective function	1
w.r.t.	x_α	Angles of attack	3
	x_{twist}	Wing twist	6
	Δz	Wing shape (FFD)	198
	L_{panel}	Panel length	214
	t_{panel}	Panel thickness	224
	t_{stiff}	Stiffener thickness	224
	λ_{stiff}	Stiffener pitch	4
	h_{stiff}	Stiffener height	114
	x_{fuel}	Fuel traction variables	55
subject to	$C_L = C_L^*$	Target lift coefficients	3
	$t/t_{\text{init}}\vert_{\text{LE}} \geq 1$	Leading edge thickness	
	$t/t_{\text{init}}\vert_{\text{TE}} \geq 1$	Trailing edge thickness	
	$t/t_{\text{init}} \geq 1$	Thickness constraints	55
	$S/S_{\text{init}} \geq 1$	Planform area constraint	1
	$\Delta z_{\text{LE}_{\text{u}}} = -\Delta z_{\text{LE}_{\text{l}}}$	Fixed leading edge	11
	$\Delta z_{\text{TE}_{\text{u}}} = -\Delta z_{\text{TE}_{\text{l}}}$	Fixed trailing edge	11
	$K \leq 0.9K_{\text{init}}$	Average curvature constraint	2
	$\text{KS}_{\text{stress}} \leq 1$	Maneuver stress	3
	$\text{KS}_{\text{buckling}} \leq 1$	Maneuver buckling	2
	$L_{\text{panel}} - x_{\text{panel}} = 0$	Panel length consistency	214
	$\lvert t_{\text{panel}_i} - t_{\text{stiff}_i} \rvert \leq 2$ mm	Minimum variance between panel and stiffener thickness	224
	$\lvert t_i - t_{i+1} \rvert \leq \Delta t_{\max}$	Thickness adjacency constraints	448
	$x_{\text{fuel}} - x_{\text{fuel}}^* = 0$	Fuel traction consistency constraints	55
	$V_{\text{wingbox}} \geq M_{\text{fuel}}/\rho_{\text{fuel}}$	Fuel volume constraint	1

Table 2 Aerostructural optimization problem objective, design variables, and constraints.

panels in each component (upper skin, lower skin, ribs, and spars) share a stiffener pitch variable. The ribs and spars each have a single design variable to control their collective stiffener height.

The panel length and fuel traction design variables are simply slack variables which are implicitly set with matching sets of consistency constraints. The panel length design variables are used in the smeared stiffener model to calculate buckling properties. As the planform of the wing changes, it is critical to ensure that the buckling properties of the panels are consistent with the updated dimensions of the panels. A set of 214 panel length consistency constraints implicitly forces an update to the panel lengths whenever the wing planform changes. Five of the skin panels on each surface of the wing are triangular patches and are incompatible with the assumptions for the panel buckling calculations. Therefore, we do not apply buckling constraints on a total of 10 panels and do not set the panel length consistency constraints on these panels either. The fuel traction variables are used to scale the fuel tractions on the skin panels so that the integrated force of all tractions is equal to the total weight of the fuel load. There are 55 fuel traction consistency constraints to ensure that the tractions are updated as the fuel load changes.

The structural constraints consist of the aggregated material failure and buckling constraints enforced at the 2.5 g maneuver flight condition. A safety factor of 1.5 is applied to both the failure and buckling constraints to provide the necessary margin of safety as required by Federal Aviation Regulations Part 25 [34]. The structural failure constraint is
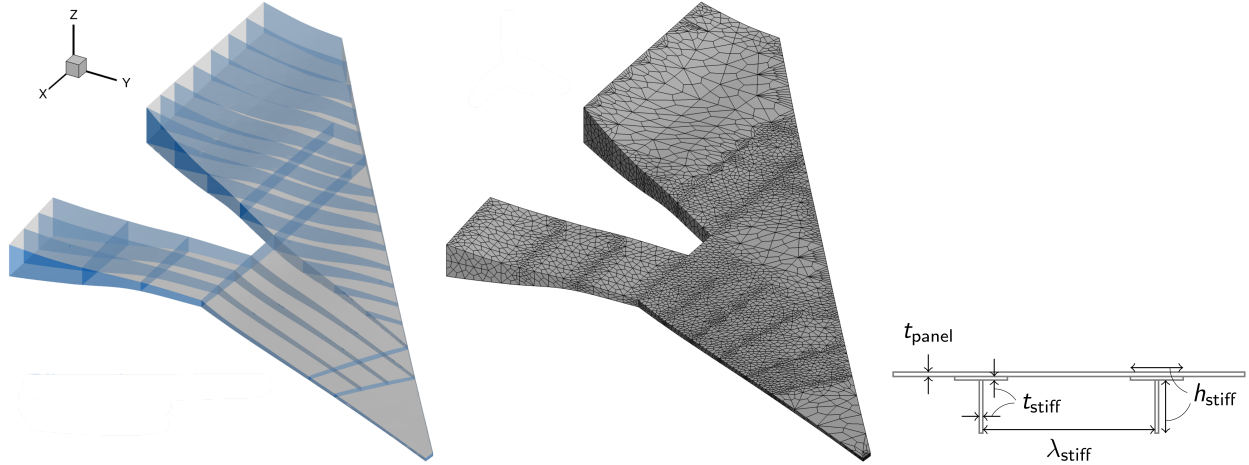
Fig. 10 The wingbox consists of a spar-rib arrangement with an bay for landing gear stowage and is discretized using quadrilateral shell elements. A smeared stiffness approach is used to model the stiffened panels.

evaluated as the ratio of the von Mises stress on the element to the material yield strength. The element-level criterion is then aggregated across the ribs and spars together, lower skin, and upper skin, resulting in a total of three failure constraints. The buckling constraint is computed similarly, with constraints aggregated across the combined ribs and spars and the upper skin. Linear adjacency constraints are enforced on the stiffener height and thickness variables to ensure that they do not vary too abruptly between adjacent panels.

4.1. Aerostructural Optimization with Fixed Planform

The first set of aerostructural optimization results correspond to the problem detailed in Table 2 except for the wing planform variables and the planform area constraint. A planform view of the upper surface C_p distributions for the transonic and supersonic conditions is shown in Fig. 11 (upper right quadrant) for $\beta = 0.75$. The drag at the transonic condition decreased by 11% relative to the baseline design for the transonic condition and by 12.6% for the supersonic condition.

The spanwise lift distributions (bottom right quadrant of Fig. 11) show how the optimizer reshaped the wing, so that it achieves a transonic lift distribution that is closer to the elliptical distribution to reduce the induced drag. As a side effect, the lift coefficients for the transonic condition near the tip increased.

In the same plot, we can see a more considerable difference between the cruise distributions and the 2.5 g maneuver distribution, where the latter is significantly reshaped to be lower in the outboard sections. This means that the optimization successfully tailored the structure to passively reduce the loads, which resulted in a structural weight decrease. One of the ways to tailor the structural stiffness is by redistributing the thickness in the wing to achieve more bend-twist coupling. We can see that this is indeed the case in the twist distribution in Fig. 11, which shows how the optimized wing twists more at the maneuver condition than the baseline design.

The streamwise lift distribution shows how the shape optimization smoothed out this distribution to reduce the lift-induced wave drag. This was achieved through airfoil shaping, as we explain later.

The airfoil sections, shown in Fig. 12, exhibit the same thickening of the two inboard sections to compensate for the lack of nacelles in the area ruling. This thickening is beneficial from the structural point of view as well. However, the middle section (at $y = 5.67$) does not thin as much as the aerodynamic case, most probably because of the structural weight benefit outweighs the aerodynamic drag in terms of the range. The thickness constraints at the wingtip are active, preventing the optimizer from reducing the wingtip thickness below that of the baseline geometry.

4.2. Aerostructural Optimization with Variable Planform

The second set of aerostructural optimization results correspond to the problem detailed in Table 2 with all the listed variables and constraints. The planform design variables are span and taper. However, sweep changes indirectly as well.
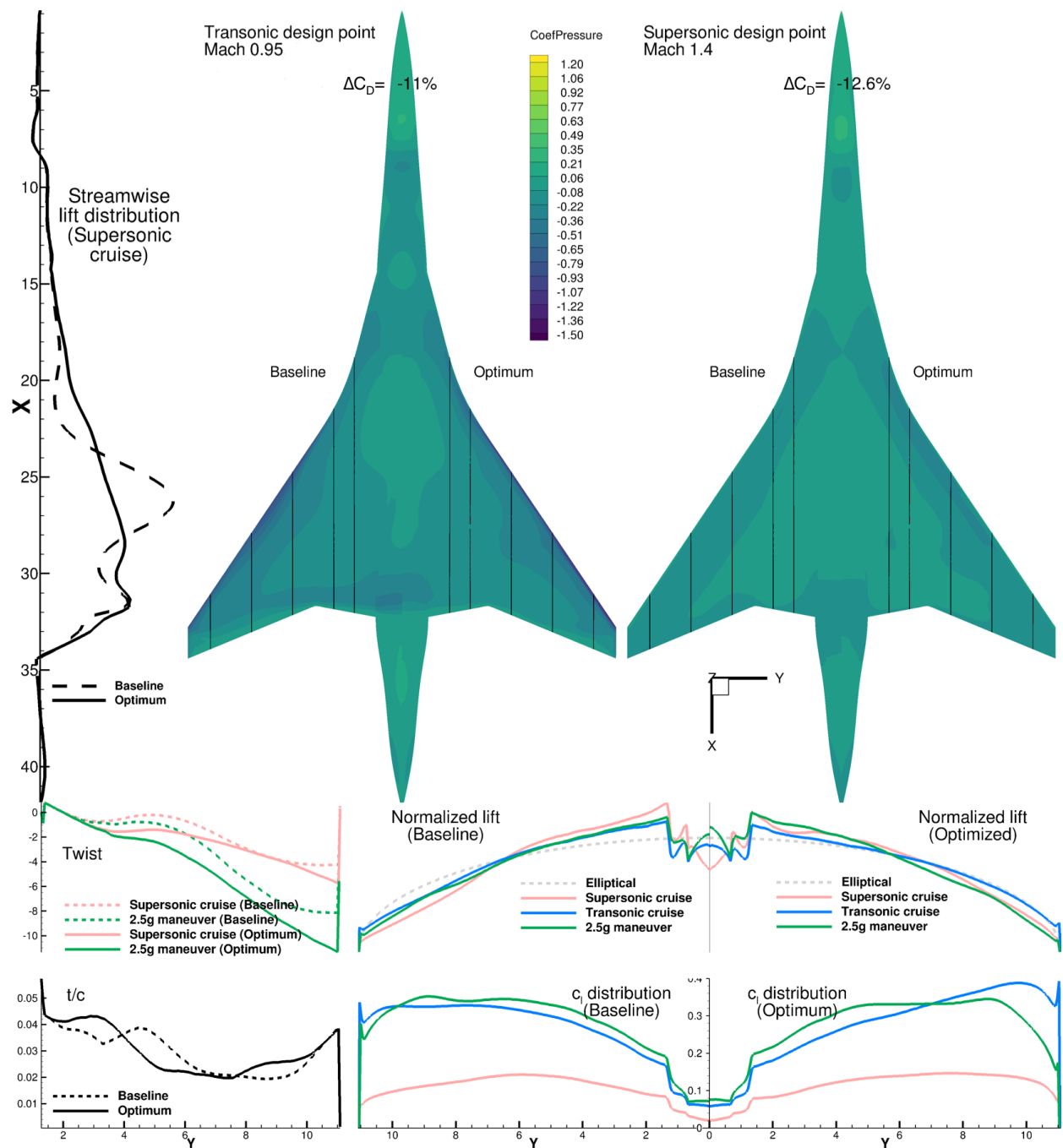
Fig. 11 Aerostructural optimization results with fixed wing planform.
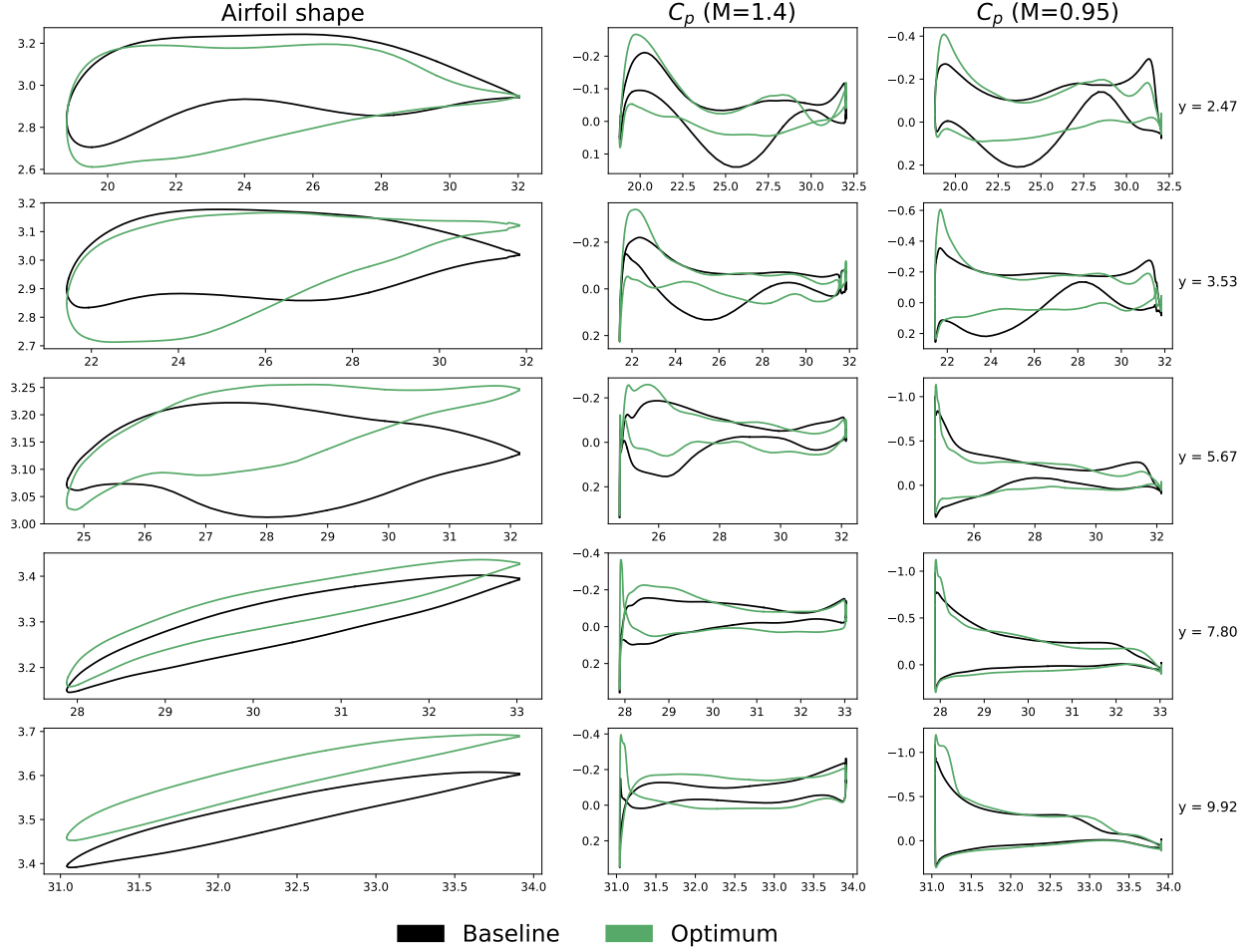
Fig. 12   Airfoil sections and pressure distributions for aerostructural optimization results with fixed wing planform.

Because of how the span variable is implemented, the sweep decreases as the span increases.

With these additional design variables, the optimization reduced the drag even more than the fixed planform case (17.8% reduction in transonic drag and 10.6% reduction in supersonic drag for $\beta = 0.75$). Overall, the optimal design features shown in Fig. 13 are similar to the fixed planform case. The main difference is that the optimization increased the span, reduced the sweep, and reduced the taper. The reduction in taper caused a higher tip lift coefficient at the transonic cruise condition. The resulting wing is more flexible than the fixed planform result and exhibits even more bend-twist coupling and thus more aggressive static aeroelastic tailoring.

The airfoil sections in Fig. 14 also show this flexibility and otherwise similar trends to the fixed planform case, including the thickening of the inboard sections. However, the midspan airfoil section ($y = 6.15$) is thinner than the one at a similar relative spanwise position in the fixed planform case. This is likely because, as observed above, the variable planform case exhibits more load alleviation, and therefore, the aerostructural trade allows for a thinner section at this spanwise position.
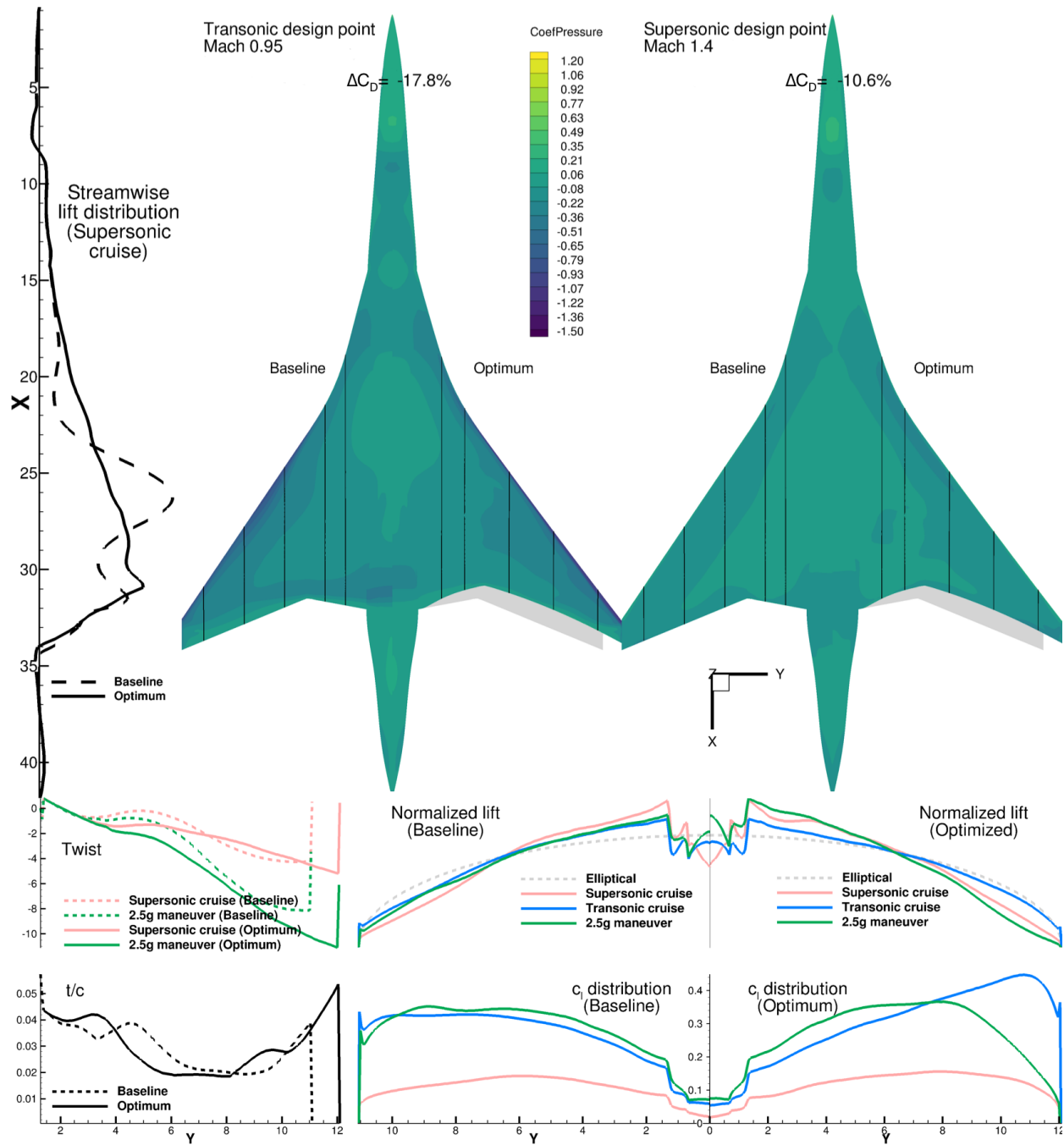
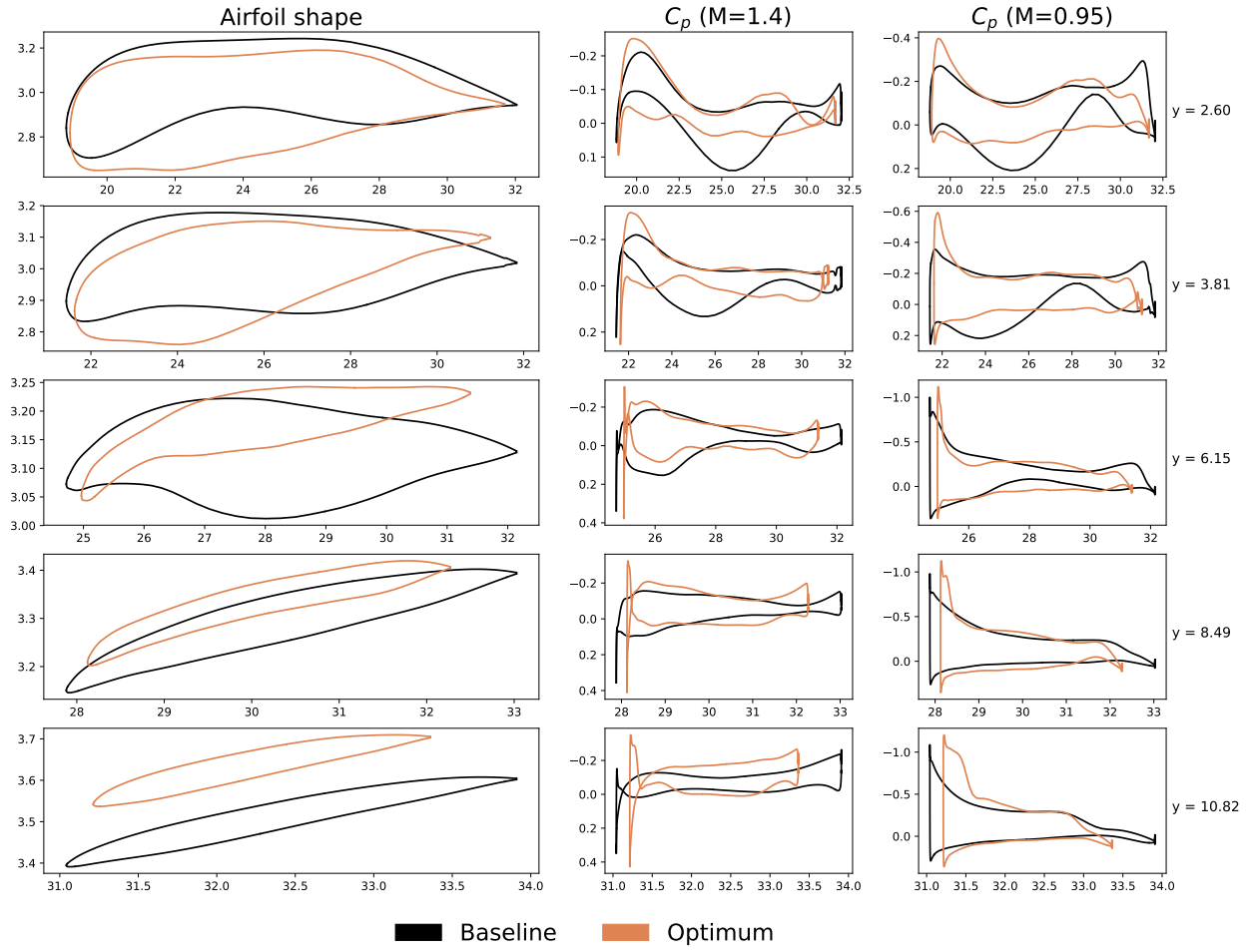**Fig. 13 Aerostructural optimization results including wing planform variables.**

Fig. 14   Airfoil sections and pressure distributions for aerostructural optimization results including wing planform variables.

4.3. Optimal Trades Between Supersonic and Transonic Performance

We study optimal trades between supersonic and transonic performance by performing a series of optimization with different values of β in the objective functions. We performed three sets of optimizations corresponding to aerodynamic shape optimization (described in Sec. 3), aerostructural optimization with fixed planform (Sec. 4.1), and aerostructural optimization with variable planform (Sec. 4.2). The values for β and the corresponding optimized ranges are listed in Table 3. The range values should not be considered to be the actual values for the Aerion AS2 because of limitations in our models (such as the lack of nacelles and an approximated specific fuel consumption).

$\beta =$	0	0.25	0.5	0.75	0.85	0.95	1
Aerodynamic	(3702, 6141)	(4256, 6137)	(4322, 6110)	–	(4361, 5961)	–	(4446, 4914)
Aerostructural (fixed plan.)	–	(4215, 6108)	(4324, 6048)	(4387, 5972)	–	–	(4430, 5018)
Aerostructural (var. plan.)	–	(3608, 7344)	(3885, 7208)	(4283, 6443)	(4385, 5990)	(4418, 5662)	(4443, 4872)

Table 3   Range data from Fig.15; (supersonic range, transonic range), in nautical miles.
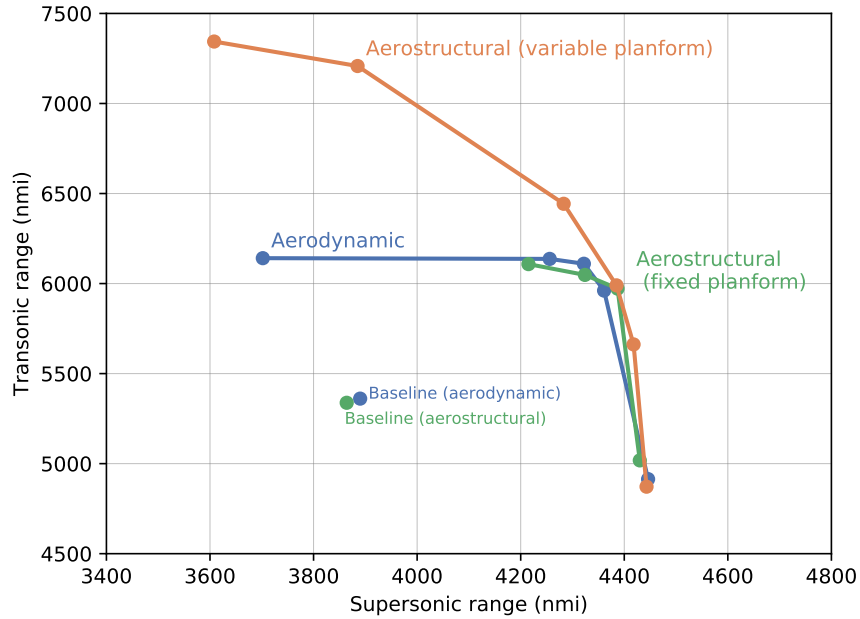

Fig. 15   Optimal trades between supersonic and transonic range for aerodynamic and aerostructural optimization.

The supersonic and transonic ranges for all optimized designs are plotted as Pareto fronts in Fig. 15. The ranges for the baseline configuration are also plotted in this figure: The two points correspond to the ranges computed with aerodynamics alone (rigid wing) and aerostructural analysis (accounting for static aeroelastic deflections at the respective cruise conditions). The difference between these two points indicates how the wing flexibility affects the performance for a given design: it decreases the supersonic range by 0.2% and the transonic range by 1.8%.

The objective of the aerodynamic shape optimization results is to minimize drag, not maximize the range. Still, we computed the ranges using the Breguet range equation (6) using the weight values for the baseline aerostructural design.

The aerodynamic optimizations significantly increased the range relative to the baseline design—up to 15% increase in supersonic range and up to 13% increase in transonic range. Part of these increases can be explained by the fact that the baseline area ruling accounted for the nacelles, and we did not consider them in these optimizations. The Pareto front shows that going from $\beta = 1$ to $\beta = 0.85$, we can trade a decrease of 2% in the supersonic range for an increase of 17% in the transonic range. For $\beta < 0.5$, the trade is less favorable and the gains in transonic range become negligible

for $\beta < 0.25$.

The aerostructural optimizations with fixed planform show a similar trend to the aerodynamic optimizations, but we optimized for a slightly different set of β values. Going from $\beta = 1$ to $\beta = 0.75$, we can trade 1% decrease in supersonic range for a 16% increase in transonic range. Further emphasis on transonic range offers diminishing returns, as we can see from the flattening of the Pareto front. Comparing the leftmost point ($\beta = 0.25$) with the corresponding aerodynamic optimum, we can see an offset that is consistent with the baseline differences between the rigid and flexible cases, showing a decrease in both the supersonic and transonic ranges. It is not fair to compare the whole aerodynamic Pareto front directly with the aerostructural ones because we assumed a fixed structural weight when computing the range for the aerodynamic designs that might not be structurally feasible for some values of β. Nevertheless, the knee of the Pareto front for the aerostructural optimizations shows better performance than the aerodynamic optimizations for both conditions. With the aerostructural optimizations, we can resize the structure and also take advantage of static aeroelastic tailoring to reduce the structural weight.

Adding planform design variables enables us to trade between supersonic and transonic ranges more effectively. Overall, the transonic range can be increased by 51% by reducing the supersonic range by 19%. The difference is much more dramatic for lower values of β (with more emphasis on transonic performance). The reason for this can be seen by looking at the resulting wing planform shapes (Fig. 16). Recall that sweep is not one of the design variables in our parametrization, but changes indirectly with changes in span. For lower values of β, the optimizer can simultaneously increase the span and sweep. The span increase has a beneficial effect on transonic induced drag, and the sweep decrease reduces the wing weight. The area is kept constant by decreasing the tip chord. For the higher values of β (with more emphasis on supersonic performance), there is only so much the sweep can increase through shortening the span. The thickness constraints at the wingtip are active, preventing the optimizer from reducing the wingtip thickness further. This prevents us from pushing the Pareto front to higher supersonic range.
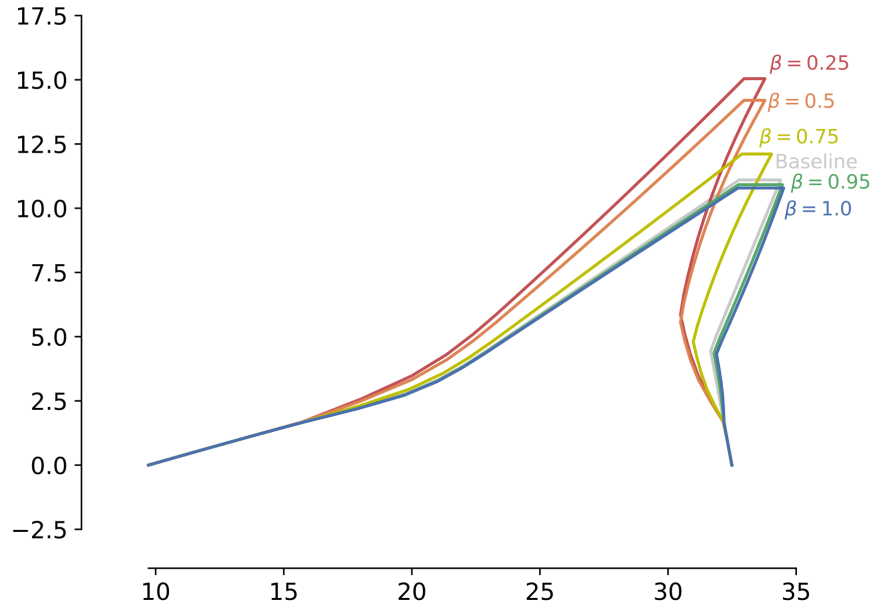

Fig. 16   Optimal planforms for different objective functions, from pure supersonic range maximization ($\beta = 1$) to increasing emphasis on transonic range (lower values of β).

By visual inspection of the Pareto front for the aerostructural optimizations with variable planform in Fig. 15, the point at $\beta = 0.85$ is the knee of the curve, representing the best tradeoff between the performance at the two flight conditions. It is not a coincidence that this point is close to the fixed planform results for $\beta = 0.75$, both in terms of performance and the wing planform shape itself. This means that the baseline wing planform was already near the optimal trade point between the supersonic and transonic range.

5. Conclusions

In this work, we presented the first of a series of CFD-based aerostructural optimization studies of the Aerion AS2 configuration with the MACH framework. The optimizations progressed from aerodynamic optimization with respect to twist and shape variables, aerostructural optimization that added structural sizing variables, and finally, aerostructural optimization with wing planform variables.

The aerostructural optimizations successfully explored tradeoffs between aerodynamics and structures. This lead to wings exhibiting passive load alleviation through static aeroelastic tailoring. The inclusion of wing planform design variables was made possible by aerostructural optimization because the optimum values for these variables require both aerodynamic and structural design considerations. This opened up the design space to trades that would not otherwise be possible.

Multipoint optimization allowed us to consider both supersonic and transonic cruise performance. Transonic performance is an essential consideration for the Aerion AS2 because of overland flight. While we had a good idea of the Mach numbers for each of these two cruise conditions, we did not know a priori how much emphasis to put on each condition and how it would impact the performance. This lead to a multiobjective optimization problem and Pareto fronts for each of the three types of optimizations (aerodynamic, aerostructural with fixed planform, and aerostructural with variable planform). We performed a total of 5 aerodynamic and 10 aerostructural optimizations to obtain the Pareto fronts.

We showed that the transonic performance could significantly increase through a small sacrifice in supersonic performance for all three types of optimization and established the limit in supersonic performance. The aerostructural optimization with planform variables resulted in an overall improvement of the Pareto front, pushing it to higher supersonic and transonic ranges. However, it enabled much larger increases in the transonic range than for supersonic range. This is partly due to the limitation in the wing planform parametrization we used, which did not explicitly include sweep. The best tradeoff between the supersonic and transonic range for the variable planform case was almost coincident with the best tradeoff point for the fixed planform case, which indicates that the baseline planform was already close to optimal.

Overall, the MACH framework allowed us to explore the wing design space much more strategically, enabling us to learn more for a given computational budget. Each aerodynamic optimization required about 1,500 CPU hours, which would mean a turn around time of a few hours with a large enough number of cores. The aerostructural optimizations with planform variables required about 10,000 CPU hours each, making overnight turn around possible.

6. Future Work

There are some limitations in the model and optimization problem formulation. The results presented here were finalized in August 2019, and work is ongoing on various improvements and follow up studies. Since there was no explicit sweep design variable parameterizing the planform, adding one or more sweep variables would be the most obvious improvement. However, sweep strongly affects the low-speed performance as well as the takeoff and landing field length, so there is a need for developing the appropriate constraints for optimization. One promising lead is the inclusion of a flow separation constraint for a low-speed condition [35]. There is also the issue of stability and control at these low-speed conditions.

Another obvious improvement would be to add the nacelles, possibly with a powered boundary condition [36]. This would avoid the dramatic thickening of certain areas in the baseline outer mold line, and would open the door to reducing wave drag by shaping the wing and possibly the nacelle to take advantage of favorable interference.

One more possibility for future work related to area ruling would be to add fuselage shape design variables. This would allow the simultaneous optimization with wing design variables (and possibly nacelle shape) to generate an optimal area ruling for the full configuration. (In the previously mentioned Aerion-inspired high-fidelity aerostructural optimization, fuselage camber variables were included, leading to a redistribution of the lift in the longitudinal axis to reduce lift-induced wave drag [17].) To include fuselage shape variables, we would have to add packaging constraints, which we have already developed and demonstrated [37].

The addition of the surface curvature constraint resulted in more reasonable shapes with a negligible adverse effect on total drag. A study of the trade between curvature and drag determined the amount of allowable curvature for this case. However, the local curvature metric was an average of the two principal curvatures, which was then averaged over each surface. A better metric would be a minimum radius, which we would constrain using constraint aggregation [38].

For the structural sizing, we included only one maneuver condition. A more realistic structural design would require many more load conditions. Also, the smeared thickness approach is an approximation that needs to be validated by a

more detailed structural analysis. Furthermore, dynamic aeroelastic phenomena, such as flutter, were not considered. Recent developments have made it possible to perform wing planform optimization considering flutter constraints [39].

These directions of possible improvement pave the way for more realistic design optimization capability. Nevertheless, we have obtained meaningful design trends and gained insights from the optimizations presented herein that can inform a more detailed design effort.

Acknowledgments

References

[1] Jetcraft, "2019 Business Aviation Market Forecast," , 2019.

[2] Sturdza, P., Manning, V. M., Kroo, I. M., and Tracy, R. R., "Boundary Layer Calculations for Preliminary Design of Wings in Supersonic Flow," *Proceedings of the 17th Applied Aerodynamics Conference*, 1999. doi:10.2514/6.1999-3104.

[3] Sturdza, P., "Extensive Supersonic Natural Laminar Flow on the Aerion Business Jet," *Proceedings of the 45th AIAA Aerospace Sciences Meeting and Exhibit*, Reno, NV, 2007. doi:10.2514/6.2007-685.

[4] Rodriguez, D., "Propulsion/Airframe Integration and Optimization on a Supersonic Business Jet," *Proceedings of the 45th AIAA Aerospace Sciences Meeting and Exhibit*, 2007. doi:10.2514/6.2007-1048.

[5] Garzon, A., and Matisheck, J., "Supersonic Testing of Natural Laminar Flow on Sharp Leading Edge Airfoils. Recent Experiments by Aerion Corporation," *In Proceedings of the 42nd AIAA Fluid Dynamics Conference and Exhibit*, 2012. doi:10.2514/6.2012-3258.

[6] Sturdza, P., and Rajnarayan, D. G., "Design and Validation of a Supersonic Natural Laminar Flow Test Article," *Proceedings of the 15th AIAA/ISSMO Multidisciplinary Analysis and Optimization Conference*, 2014. doi:10.2514/6.2014-2176.

[7] Liebhardt, B., Lütjens, K., Tracy, R. R., and Haas, A. O., "Exploring the Prospect of Small Supersonic Airliners—A Case Study Based on the Aerion AS2 Jet," *Proceedings of the 17th AIAA Aviation Technology, Integration, and Operations Conference*, 2017. doi:10.2514/6.2017-3588.

[8] Davis, Z., Carrigan, T. J., Wyman, N., and McMullen, M., "Reducing the Computational Cost of Viscous Mesh Adaptation," *Proceedings of the 23rd AIAA Computational Fluid Dynamics Conference*, 2017. doi:10.2514/6.2017-3109.

[9] McMullen, M., Shah, S., and Rajmohan, N., "Methodology for a Robust Interactive Boundary Layer Solver," *In Proceedings of the AIAA Aviation 2019 Forum*, 2019. doi:10.2514/6.2019-3040.

[10] Mukundakrishnan, B., Rajmohan, N., Rajnarayan, D. G., and Fugal, S., "A Script-Based CAD System for Aerodynamic Design," *Proceedings of the AIAA Aviation 2019 Forum*, 2019. doi:10.2514/6.2019-3069.

[11] Norris, G., "Supersonic Evolution," *Aviation Week & Space Technology*, 2020, pp. 50–54.

[12] Plotkin, K., Matisheck, J., and Tracy, R., "Sonic Boom Cutoff Across the United States," *Proceedings of the 14th AIAA/CEAS Aeroacoustics Conference*, 2008. doi:10.2514/6.2008-3033.

[13] Kenway, G. K. W., and Martins, J. R. R. A., "Multipoint Aerodynamic Shape Optimization Investigations of the Common Research Model Wing," *AIAA Journal*, Vol. 54, No. 1, 2016, pp. 113–128. doi:10.2514/1.J054154.

[14] Mangano, M., and Martins, J. R. R. A., "Multipoint Aerodynamic Shape Optimization for Subsonic and Supersonic Regimes," *Journal of Aircraft*, 2020. (In press).

[15] Kenway, G. K. W., and Martins, J. R. R. A., "Multipoint High-Fidelity Aerostructural Optimization of a Transport Aircraft Configuration," *Journal of Aircraft*, Vol. 51, No. 1, 2014, pp. 144–160. doi:10.2514/1.C032150.

[16] Kenway, G. K. W., Kennedy, G. J., and Martins, J. R. R. A., "Scalable Parallel Approach for High-Fidelity Steady-State Aeroelastic Analysis and Derivative Computations," *AIAA Journal*, Vol. 52, No. 5, 2014, pp. 935–951. doi:10.2514/1.J052255.

[17] Martins, J. R. R. A., Alonso, J. J., and Reuther, J. J., "High-Fidelity Aerostructural Design Optimization of a Supersonic Business Jet," *Journal of Aircraft*, Vol. 41, No. 3, 2004, pp. 523–530. doi:10.2514/1.11478.

[18] Liem, R. P., Kenway, G. K. W., and Martins, J. R. R. A., "Multimission Aircraft Fuel Burn Minimization via Multipoint Aerostructural Optimization," *AIAA Journal*, Vol. 53, No. 1, 2015, pp. 104–122. doi:10.2514/1.J052940.

[19] Mader, C. A., Kenway, G. K., Martins, J. R. R. A., and Uranga, A., "Aerostructural Optimization of the D8 Wing with Varying Cruise Mach Numbers," *18th AIAA/ISSMO Multidisciplinary Analysis and Optimization Conference*, American Institute of Aeronautics and Astronautics, 2017. doi:10.2514/6.2017-4436.

[20] Burdette, D. A., and Martins, J. R. R. A., "Design of a Transonic Wing with an Adaptive Morphing Trailing Edge via Aerostructural Optimization," *Aerospace Science and Technology*, Vol. 81, 2018, pp. 192–203. doi:10.1016/j.ast.2018.08.004.

[21] Burdette, D. A., and Martins, J. R. R. A., "Impact of Morphing Trailing Edge on Mission Performance for the Common Research Model," *Journal of Aircraft*, Vol. 56, No. 1, 2019, pp. 369–384. doi:10.2514/1.C034967.

[22] Brooks, T. R., Martins, J. R. R. A., and Kennedy, G. J., "High-fidelity Aerostructural Optimization of Tow-steered Composite Wings," *Journal of Fluids and Structures*, Vol. 88, 2019, pp. 122–147. doi:10.1016/j.jfluidstructs.2019.04.005.

[23] Brooks, T. R., Martins, J. R. R. A., and Kennedy, G. J., "Aerostructural Trade-offs for Tow-steered Composite Wings," *Journal of Aircraft*, 2020. doi:10.2514/1.C035699.

[24] Mader, C. A., Kenway, G. K. W., Yildirim, A., and Martins, J. R. R. A., "ADflow—An open-source computational fluid dynamics solver for aerodynamic and multidisciplinary optimization," *Journal of Aerospace Information Systems*, 2020. doi:10.2514/1.I010796.

[25] Kenway, G. K. W., Mader, C. A., He, P., and Martins, J. R. R. A., "Effective Adjoint Approaches for Computational Fluid Dynamics," *Progress in Aerospace Sciences*, Vol. 110, 2019, p. 100542. doi:10.1016/j.paerosci.2019.05.002.

[26] Kennedy, G. J., and Martins, J. R. R. A., "A Parallel Finite-Element Framework for Large-Scale Gradient-Based Design Optimization of High-Performance Structures," *Finite Elements in Analysis and Design*, Vol. 87, 2014, pp. 56–73. doi:10.1016/j.finel.2014.04.011.

[27] Uyttersprot, L., "Inverse Distance Weighting Mesh Deformation," Ph.D. thesis, Delft University of Technology, 2014.

[28] Brown, S. A., "Displacement Extrapolation for CFD+CSM Aeroelastic Analysis," *Proceedings of the 35th AIAA Aerospace Sciences Meeting*, Reno, NV, 1997. AIAA 1997-1090.

[29] Martins, J. R. R. A., Alonso, J. J., and Reuther, J. J., "A Coupled-Adjoint Sensitivity Analysis Method for High-Fidelity Aero-Structural Design," *Optimization and Engineering*, Vol. 6, No. 1, 2005, pp. 33–62. doi:10.1023/B:OPTE.0000048536.47956.62.

[30] Perez, R. E., Jansen, P. W., and Martins, J. R. R. A., "pyOpt: A Python-Based Object-Oriented Framework for Non-linear Constrained Optimization," *Structural and Multidisciplinary Optimization*, Vol. 45, No. 1, 2012, pp. 101–118. doi:10.1007/s00158-011-0666-3.

[31] Chen, S., Lyu, Z., Kenway, G. K. W., and Martins, J. R. R. A., "Aerodynamic Shape Optimization of the Common Research Model Wing-Body-Tail Configuration," *Journal of Aircraft*, Vol. 53, No. 1, 2016, pp. 276–293. doi:10.2514/1.C033328.

[32] Secco, N. R., Jasa, J. P., Kenway, G. K. W., and Martins, J. R. R. A., "Component-based Geometry Manipulation for Aerodynamic Shape Optimization with Overset Meshes," *AIAA Journal*, Vol. 56, No. 9, 2018, pp. 3667–3679. doi:10.2514/1.J056550.

[33] Brooks, T. R., , and Martins, J. R. R. A., "High-fidelity Aerostructural Optimization Considering Manufacturing Cost," Presentation, December 2016.

[34] Federal Aviation Administration, "Federal Aviation Regulations, Part 25 — Airworthiness Standards: Transport Category Airplanes," , Feb. 2009. URL http://www.faa.gov/regulations_policies/.

[35] Bons, N. P., "High-fidelity Wing Design Exploration with Gradient-based Optimization," Ph.D. thesis, University of Michigan, Ann Arbor, MI, May 2020.

[36] Gray, J. S., and Martins, J. R. R. A., "Coupled Aeropropulsive Design Optimization of a Boundary-Layer Ingestion Propulsor," *The Aeronautical Journal*, Vol. 123, No. 1259, 2019, pp. 121–137. doi:10.1017/aer.2018.120.

[37] Brelje, B. J., Anibal, J., Yildirim, A., Mader, C. A., and Martins, J. R. R. A., "Flexible Formulation of Spatial Integration Constraints in Aerodynamic Shape Optimization," *AIAA Journal*, 2020. (In press).

[38] Lambe, A. B., Martins, J. R. R. A., and Kennedy, G. J., "An Evaluation of Constraint Aggregation Strategies for Wing Box Mass Minimization," *Structural and Multidisciplinary Optimization*, Vol. 55, No. 1, 2017, pp. 257–277. doi:10.1007/s00158-016-1495-1.

[39] Jonsson, E., Riso, C., Lupp, C. A., Cesnik, C. E. S., Martins, J. R. R. A., and Epureanu, B. I., "Flutter and Post-Flutter Constraints in Aircraft Design Optimization," *Progress in Aerospace Sciences*, Vol. 109, 2019, p. 100537. doi:10.1016/j.paerosci.2019.04.001.